Journal of Power Sources 196 (2011) 4923–4933

Contents lists available at ScienceDirect

Journal of Power Sources

journal homepage: www.elsevier.com/locate/jpowsour

Effects of property variation and ideal solution assumption on the calculation of the limiting current density condition of alkaline fuel cells

Ge Zhou[a,1], Lea-Der Chen[a,*,2], James P. Seaba[b]

[a] Department of Mechanical and Industrial Engineering, The University of Iowa, Iowa City, IA 52242, USA
[b] ConocoPhillips Co., 240 PLB, Bartlesville Technology Center, Bartlesville, OK 74004, USA

ARTICLE INFO

Article history:
Received 11 January 2011
Received in revised form 3 February 2011
Accepted 4 February 2011
Available online 12 February 2011

Keywords:
Alkaline fuel cell
Ideal solution
Property effect
Limiting current density

ABSTRACT

A computational study of the electrochemical hydrodynamic process in an alkaline fuel cell was conducted. The computation relaxed the ideal solution assumption, accounted for thermodynamic solubility of the reactants, and allowed for property variations due to temperature and concentration effects. The results showed that the ideal solution assumption is not adequate for calculation of the transport process of the concentrated electrolyte considered, 7 M. The ideal solution formulation resulted in a lower limiting current density condition by about 50% than that predicted by the non-ideal solution formulation. The study also showed that the thermal condition is important to the calculation of the limiting current density condition. The calculated limiting current density increased by about 30% when the boundary condition was changed from isothermal to adiabatic. The computational results suggest that maintaining a uniform KOH concentration in the electrolyte (for example, at design point of 7 M) be an effective measure to increase the limiting current density condition.

© 2011 Elsevier B.V. All rights reserved.

1. Introduction

Stationary fuel cell is a viable option for electrical power generation from renewable sources. For example, H_2 produced by solar or wind turbine based electrolysis can be used to fuel the fuel cells. Among the fuel cell platforms, alkaline fuel cell (AFC) remains a good prospect as it has high reliability and it can use non-precious metal for the electrodes [1–6,23]. However, to be competitive with other power sources, the power density (as well as the cost of manufacturing, operation and maintenance) needs to be improved. A CFD based study of the electrochemical hydrodynamic process that sets the limiting current density condition is conducted. The purpose of this study is to gain a better understanding of the mechanisms critical to setting the limiting current density condition, and to demonstrate the application of CFD based simulation to aid design consideration.

The CFD formation accounts for the electrochemical reaction, charge and species transport, and thermodynamics of gas solubility in the electrolyte. The mathematical models that describe the transport processes are available in the literature, e.g., see [7–13]. However, most transport models were based upon the assumption of ideal solution for the calculation of the transport properties. Error associated with the ideal solution assumption was not assessed. Furthermore, most CFD studies reported in literature assumed an isothermal system. The temperature effects were not evaluated. In this paper, the ideal solution assumption was relaxed and the temperature effects were examined. The objectives of this paper are (a) to examine the effects on CFD calculation due to the ideal solution and isothermal assumptions, and (b) to gain insights into the mechanisms that are critical to setting the limiting current density condition.

2. Formulation

2.1. Transport equations

Major assumptions invoked are (a) Newtonian fluid, (b) negligible pressure effects on enthalpy, (c) negligible magnetic effects due to electrical field, (d) negligible pressure and temperature effects on diffusion transport, (e) negligible viscous dissipation, pressure work, and Dufour effects in energy equation, (f) no homogeneous chemical reactions, (g) electroneutrality, (h) homogeneous and continuous media for gas and liquid phase, (i) local thermal equilibrium, (j) vapor–liquid equilibrium at the gas–liquid interface, and (k) negligible electrical resistance of the electrodes. The governing equations describing the transport of mass, momentum, species, energy and charge balance are summarized in Table 1. The

* Corresponding author. Tel.: +1 361 825 3046; fax: +1 361 825 3056.
E-mail address: ldchen@tamucc.edu (L.-D. Chen).
[1] Currently with UTC Power, 195 Governor's Highway, South Windsor, CT 06074, USA.
[2] Currently with Texas A&M University – Corpus Christi, Corpus Christi, TX 78412, USA.

0378-7753/$ – see front matter © 2011 Elsevier B.V. All rights reserved.
doi:10.1016/j.jpowsour.2011.02.026

Nomenclature

a_k	activity of species k
$a_{\beta\gamma}$	specific interfacial area between phase β (liquid) and phase γ (gas) (m^{-1})
$a_{\beta\sigma}$	specific interfacial area between phase β (liquid) and phase σ (solid) (m^{-1})
C_k	molar concentration of species k ($kmol\,m^{-3}$)
C_p	specific heat ($J\,kg^{-1}\,K^{-1}$)
D_k	diffusion coefficient of species k into the solution/mixture ($m^2\,s^{-1}$)
D_{kj}	multicomponent Maxwell–Stefan binary diffusion coefficient ($m^2\,s^{-1}$)
d_f	fiber diameter (m)
E	electric potential (V)
F	Faraday constant ($C\,kmol^{-1}$)
$\boldsymbol{g}$	gravitational acceleration ($m\,s^{-2}$)
H	Henry's constant ($kmol\,m^{-3}\,atm^{-1}$)
i	current density ($A\,m^{-2}$)
i_0	exchange current density ($A\,m^{-2}$)
$\boldsymbol{i}$	vector quantity of current density ($A\,m^{-2}$)
i_n	current density at solid–liquid interface ($A\,m^{-2}$)
$\boldsymbol{j}_k$	vector quantity of mass flux of species k ($kg\,m^{-2}\,s^{-1}$)
K	absolute permeability (m^2)
k^r	relative permeability
k_K	Kozeny constant
k_{scx}	Setschenow salt effect parameter
M_k	molecular weight of species k ($kg\,kmol^{-1}$)
m	molality ($mol\,kg^{-1}$)
n	number of electron transfer
p	pressure (Pa)
p_c	capillary pressure (Pa)
p_s	saturation vapor pressure (Pa)
q_k	stoichiometric coefficient of species k
R_u	universal gas constant ($J\,kmol^{-1}\,K^{-1}$)
S	entropy ($J\,kmol^{-1}\,K^{-1}$)
S_r	reduced phase saturation
s	saturation
s_{im}	immobile saturation
s_k	stoichiometric coefficient of species k
T	temperature (K)
t	time (s)
t_k	transference number of species k
U	open cell potential (V)
u_k	mobility of species k ($m\,s^{-1}\,kmol\,N^{-1}$)
$\boldsymbol{v}$	velocity vector ($m\,s^{-1}$)
x_k	mole fraction of species k
Y_k	mass fraction of species k
z_k	charge number of species k

Greek

α	transfer coefficient
δ	film thickness (m)
$\gamma_{\pm,C}$	mean activity coefficient based on molarity
ε	porosity
η	local overpotential (V)
κ	electrical conductivity ($S\,m^{-1}$)
κ^D	diffusion conductivity ($A\,m^{-1}$)
λ	thermal conductivity ($W\,m^{-1}\,K^{-1}$)
λ_k^0	limiting ionic equivalent conductance of ion k ($S\,m^2\,kmol^{-1}$)
μ	dynamic viscosity ($kg\,s^{-1}\,m^{-1}$)
μ_k	chemical potential of species k ($J\,kmol^{-1}$)
υ	stoichiometric coefficient
υ_k	number of cation or anion produced by the dissociating electrolyte
θ_c	contact angle
ρ	density ($kg\,m^{-3}$)
σ	surface tension ($N\,m^{-1}$)
τ	normal or shear stress ($N\,m^{-2}$)
Φ	electric potential at electrolyte phase (V)

Subscripts

a	anode
c	cathode
e	electrolyte
g	gas
i,j,k	species
l	liquid
m	mixture
nw	non-wetting
T	total
w	wetting
β	liquid phase
γ	gas phase
σ	solid phase
0	standard state, pressure at 1 atm or solvent or reference value
+	cation
−	anion

Superscripts

a	anode
c	cathode
eff	effective
h	energy
i	charge
m	mass
r	reference state
β	liquid phase
γ	gas phase
σ	solid phase
0	standard state, pressure at 1 atm, or solvent/reference state

respective source terms are given in Table 2. The source terms account for (a) mass and species addition or removal due to gas solubility and H_2O phase change, (b) momentum exchange due to Darcian flow in porous electrodes, (c) energy source or sink terms due to heat and entropy generation at catalyst layer, Joule heating in separator and catalyst layer, and latent heat of H_2O phase change, and (d) charge generation at catalyst layer. The constitutive equations describing the reaction rate (Butler–Volmer equation), capillary pressure (Leverett–J function), and physical properties are given in Table 3. Conservation equation of the liquid-phase species is solved only for OH^-. The mass fraction of K^+ is calculated from electroneutrality.

2.2. Electrochemical reaction

One-step electrochemical reactions are assumed for anode and cathode electrodes,

Anode:

$$H_2 + 2OH^- \rightarrow 2H_2O + 2e^- \quad (1)$$

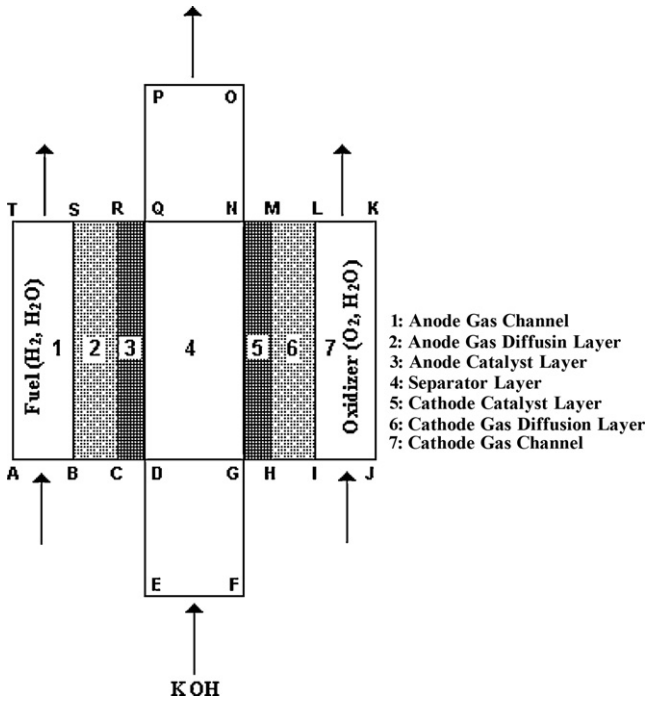

Fig. 1. Schematic of alkaline fuel cell.

Cathode:

$$O_2 + 2H_2O + 4e^- \rightarrow 4OH^- \quad (2)$$

The anode and cathode half cell voltage is calculated by

$$E_a = U_a + \eta_a + \Phi_a \quad (3)$$

$$E_c = U_c + \eta_c + \Phi_c \quad (4)$$

where subscripts a and c denote anode and cathode, respectively. The overall cell voltage is obtained from

$$E_{cell} = E_c - E_a = (U_c - U_a) + (\eta_c - \eta_a) + (\Phi_c - \Phi_a) \quad (5)$$

where E is the potential of the solid phase, Φ is the potential of the liquid phase, and η is the activation overpotential. The $U_c - U_a$ term in Eq. (5) is the theoretical equilibrium cell voltage calculated from the Gibbs free energy; $\eta_c - \eta_a$ is the activation overpotential, and $\Phi_c - \Phi_a$ is the potential drop due to the concentration overpotential and IR losses. The half-cell open potential is calculated by Nernst equation:

$$U_a = U_a^0 - \left[\frac{R_u T}{n_a F}\right]\left[\ln\left(\left(\frac{p_{H_2}}{p^0_{H_2}}\right)^{s^a_{H_2}}\left(\frac{C_{OH^-}}{C^0_{OH^-}}\right)^{s^a_{OH^-}}\right)\right] \quad (6)$$

$$U_c = U_c^0 - \left[\frac{R_u T}{n_a F}\right]\left[\ln\left(\frac{p_{O_2}}{p^0_{O_2}}{}^{s^c_{O_2}}\left(\frac{C_{OH^-}}{C^0_{OH^-}}\right)^{s^c_{OH^-}}\right)\right] \quad (7)$$

where U^0 is the theoretical open cell potential evaluated at standard concentration C^0 at 1 atm and given temperature T; s_k is the stoichiometric coefficient of species k; n_a is the number of electron transfer at anode. The temperature effects on theoretical open cell potential are calculated following [14]:

$$U_T^0 = U_{298}^0 + (T - 298.15)\left(\frac{dU^0}{dT}\right)_{298} \quad (8)$$

$$U_a^0 = -0.823 - (T - 298.15) \times 8.360 \times 10^{-4} \ \text{V} \quad (9)$$

$$U_c^0 = 0.4011 - (T - 298.15) \times 1.6816 \times 10^{-3} \ \text{V} \quad (10)$$

Table 1
Transport equations (β: liquid phase, γ: gas phase, σ: solid phase).

Mass

$\frac{\partial}{\partial t}\varepsilon_\beta\rho_\beta + \nabla\cdot\varepsilon_\beta\rho_\beta\boldsymbol{v}_\beta = S^m_{\beta\gamma}$

$\frac{\partial}{\partial t}\varepsilon_\gamma\rho_\gamma + \nabla\cdot\varepsilon_\gamma\rho_\gamma\boldsymbol{v}_\gamma = -S^m_{\beta\gamma}$

Momentum

$\frac{\partial}{\partial t}(\varepsilon_\beta\rho_\beta\boldsymbol{v}_\beta) + \nabla\cdot(\varepsilon_\beta\rho_\beta\boldsymbol{v}_\beta\boldsymbol{v}_\beta) = -\varepsilon_\beta\nabla p_\beta + \nabla\cdot(\mu^{eff}_\beta\nabla\boldsymbol{v}_\beta) + \varepsilon_\beta\rho_\beta\boldsymbol{g} + S^v_\beta$

$\frac{\partial}{\partial t}(\varepsilon_\gamma\rho_\gamma\boldsymbol{v}_\gamma) + \nabla\cdot(\varepsilon_\gamma\rho_\gamma\boldsymbol{v}_\gamma\boldsymbol{v}_\gamma) = -\varepsilon_\gamma\nabla p_\gamma + \nabla\cdot(\mu^{eff}_\gamma\nabla\boldsymbol{v}_\gamma) + \varepsilon_\gamma\rho_\gamma\boldsymbol{g} + S^v_\gamma$

Species

$\frac{\partial}{\partial t}(\varepsilon_\beta\rho_\beta Y_{\beta i}) + \nabla\cdot(\varepsilon_\beta\rho_\beta\boldsymbol{v}_\beta Y_{\beta i}) = \nabla\cdot(\rho_\beta D^{eff}_{\beta i}\Delta Y_{\beta i}) - \frac{M_{\beta i}}{z_{\beta i}F}\boldsymbol{i}_\beta\cdot\nabla t_{\beta i} + S^m_{\beta,i}$; $i = H_2, O_2, H_2O, OH^-$

$\frac{\partial}{\partial t}(\varepsilon_\gamma\rho_\gamma Y_{\gamma i}) + \nabla\cdot(\varepsilon_\gamma\rho_\gamma\boldsymbol{v}_\gamma Y_{\gamma i}) = \nabla\cdot(\rho_\gamma D^{eff}_{\gamma i}\Delta Y_{\gamma i}) + S^m_{\gamma,i}$; $i = H_2, O_2, H_2O$

Energy

$\rho C_p{}^{eff}\frac{\partial T}{\partial t} + (C_{p\beta}\varepsilon_\beta\rho_\beta\boldsymbol{v}_\beta + C_{p\gamma}\varepsilon_\gamma\rho_\gamma\boldsymbol{v}_\gamma)\cdot\nabla T =$
$\nabla\cdot(\lambda^{eff}\nabla T) + S^h_{react} + S^h_{phase} + S^h_{Joule}$

Charge

$\nabla\cdot(\kappa^{eff}_\beta\nabla\Phi_\beta) + \nabla\cdot(\kappa^{D,eff}_\beta\nabla\ln C_{\beta e}) = S^{\mathbf{i}}_{\beta\sigma}$

2.3. Ideal solution

The Nernst–Planck equation is used to calculate the flux of charge species in electrolyte. For ideal solution, the flux of species k is obtained from Eq. (11) [7]:

$$\boldsymbol{j}_k = -\rho D_k\nabla Y_k - \rho Y_k u_k z_k F\nabla\Phi + \rho Y_k\boldsymbol{v} \quad (11)$$

The RHS of the equation are the Fickian diffusion, migration, and convective terms, respectively. For concentrated solutions, the

Table 2
Source terms of governing equations (Table 1).

Mass transfer rate at the liquid–gas interface of catalyst layer

Anode : $S^m_{\beta\gamma} = -a_{\beta\gamma}\frac{D_{\gamma,H_2O}}{\delta_g}\left(\frac{p_s}{R_uT} - \frac{p_{H_2O}}{R_uT}\right)M_{H_2O} + a_{\beta\gamma}D_{\beta,H_2}\frac{H_{H_2}p_{H_2} - C_{H_2}}{\delta_l}M_{H_2}$

Cathode : $S^m_{\beta\gamma} = -a_{\beta\gamma}\frac{D_{\gamma,H_2O}}{\delta_g}\left(\frac{p_s}{R_uT} - \frac{p_{H_2O}}{R_uT}\right)M_{H_2O} + a_{\beta\gamma}D_{\beta,O_2}\frac{H_{O_2}p_{O_2} - C_{O_2}}{\delta_l}M_{O_2}$

Liquid-phase viscous drag

Catalyst layers : $S^v_\beta = -\frac{\varepsilon_\beta\mu_\beta\boldsymbol{v}_\beta}{K_\beta}$

GDL : $S^v_\gamma = -\frac{\varepsilon_\gamma\mu_\gamma\boldsymbol{v}_\gamma}{K_\gamma}$

Hydroxide ions reaction rate (anode catalyst layer and cathode catalyst layer)

$S^m_{\beta,OH^-} = \frac{M_{OH^-}}{z_{OH^-}F}(1 - t_{OH^-})a_{\beta\sigma}i_n$, $[anode(n = a),\ cathode(n = c)]$

Hydrogen reaction rate and dissolvation rate (anode catalyst layer)

$S^m_{\beta,H_2} = -\frac{M_{H_2}}{2F}a_{\beta\sigma}i_a + a_{\beta\gamma}D_{\beta,H_2}\frac{H_{H_2}p_{H_2} - C_{H_2}}{\delta_l}M_{H_2}$

Oxygen reaction rate and dissolvation rate (cathode catalyst layer)

$S^m_{\beta,O_2} = \frac{M_{O_2}}{4F}a_{\beta\sigma}i_c + a_{\beta\gamma}D_{\beta,O_2}\frac{H_{O_2}p_{O_2} - C_{O_2}}{\delta_l}M_{O_2}$

Hydrogen dissolvation rate (anode catalyst layer)

$S^m_{\gamma,H_2} = -a_{\beta\gamma}D_{\beta,H_2}\frac{H_{H_2}p_{H_2} - C_{H_2}}{\delta_l}M_{H_2}$

Oxygen dissolvation rate (cathode catalyst layer)

$S^m_{\gamma,O_2} = -a_{\beta\gamma}D_{\beta,O_2}\frac{H_{O_2}p_{O_2} - C_{O_2}}{\delta_l}M_{O_2}$

Water evaporation rate (anode catalyst layer and cathode catalyst layer)

$S^m_{\gamma,H_2O} = a_{\beta\gamma}\frac{D_{\gamma,H_2O}}{\delta_g}\left(\frac{p_s}{R_uT} - \frac{p_{H_2O}}{R_uT}\right)M_{H_2O}$

Charge generation rate (anode catalyst layer and cathode catalyst layer)

$S^{\mathbf{i}}_{\beta\sigma} = -a_{\beta\sigma}i_n$, $anode(n = a)$, $cathode(n = c)$

Heat source due to Joule heating (anode catalyst layer and cathode catalyst layer; separator)

$S^h_{Joule} = -i_\beta\cdot\nabla\Phi_\beta$

Heat source due to reversible and irreversible reaction heat (anode and cathode catalyst layer)

$S^h = a_{\beta\sigma}\left(i_n\eta - \frac{i_n}{nF}T\Delta S\right)$

Heat source due to phase change (anode and cathode catalyst layer)

$S^h = -S^m_{\gamma,H_2O}h_{\beta\gamma,H_2O}$

Table 3
Constitutive Equations.

Local reaction current ($A\,m^{-2}$)	$i_a = i_0^a \left[\left(\frac{C_{H_2}}{C_{H_2}^r} \right)^{q_{H_2}^a} \left(\frac{C_{OH^-}}{C_{OH^-}^r} \right)^{q_{OH^-}^a} \exp\left(\frac{\alpha_a^a n_a F \eta_a}{R_u T} \right) - \left(\frac{C_{H_2O}}{C_{H_2O}^r} \right)^{q_{H_2O}^a} \exp\left(-\frac{\alpha_c^a n_a F \eta_a}{R_u T} \right) \right]$
	$i_c = i_0^c \left[\left(\frac{C_{OH^-}}{C_{OH^-}^r} \right)^{q_{OH^-}^c} \exp\left(\frac{\alpha_a^c n_c F \eta_c}{R_u T} \right) - \left(\frac{C_{O_2}}{C_{O_2}^r} \right)^{q_{O_2}^c} \left(\frac{C_{H_2O}}{C_{H_2O}^r} \right)^{q_{H_2O}^c} \exp\left(-\frac{\alpha_c^c n_c F \eta_c}{R_u T} \right) \right]$
Effective viscosity ($kg\,m^{-1}\,s^{-1}$)	$\mu_\beta^{eff} = \frac{\varepsilon_\beta}{\tau_\beta}\mu_\beta, \quad \mu_\gamma^{eff} = \frac{\varepsilon_\gamma}{\tau_\gamma}\mu_\gamma$
Effective diffusion coefficient ($m^2\,s^{-1}$)	$D_{\beta i}^{eff} = \frac{\varepsilon_\beta}{\tau_\beta} D_{\beta i}, \quad D_{\gamma i}^{eff} = \frac{\varepsilon_\gamma}{\tau_\gamma} D_{\gamma i}$
Effective electrical conductivity ($S\,m^{-1}$)	$\kappa_\beta^{eff} = \frac{\varepsilon_\beta}{\tau_\beta}\kappa_\beta$
Effective diffusion conductivity ($A\,m^{-1}$)	$\kappa_\beta^{D,eff} = \frac{2R_u T \kappa_\beta^{eff}}{F}\left(1 - t_-^0 + \frac{C_e}{2C_0}\right)\left(1 + \frac{d\ln\gamma_{\pm,C}}{d\ln C_e}\right)$
Permeability (m^2)	$K = \frac{\varepsilon^3 d_f^2}{16k_K(1-\varepsilon)^2}, \quad k_{r,nw} = {S_r}^3, \quad k_{r,w} = (1-S_r)^3$
Capillary pressure (Pa)	$p_c = \frac{\sigma_S \cos\theta_c}{(K/\varepsilon)^{1/2}}(1.417S_r - 2.120{S_r}^2 + 1.263{S_r}^3), \quad S_r = \frac{s - s_{im}}{1 - s_{im}},$
Current flux ($A\,m^{-2}$)	$\boldsymbol{i}_\beta = -\kappa_\beta^{eff}\nabla\Phi_\beta - \kappa_\beta^{D,eff}\nabla\ln C_{\beta e}$
Effective thermal conductivity ($W\,m^{-1}\,K^{-1}$)	$\lambda^{eff} = \varepsilon_\beta\lambda_\beta + \varepsilon_\gamma\lambda_\gamma + \varepsilon_\sigma\lambda_\sigma$
Specific heat ($J\,kg^{-1}\,K^{-1}$)	$C_p{}^{eff} = (\varepsilon_\beta\rho_\beta C_{p\beta} + \varepsilon_\gamma\rho_\gamma C_{p\gamma} + \varepsilon_\sigma\rho_\sigma C_{p\sigma})/\sigma$
Electrical potential (V)	$\Phi_\sigma^a = 0, \quad \Phi_\sigma^c = E_{cell}$

generalized Stefan–Maxwell equation is used [7,15]:

$$\sum_{\substack{i=1 \\ i\neq k}}^{N} \left(\frac{x_k x_i}{D_{ki}}\right)\left(\frac{\boldsymbol{j}_i}{\rho_i} - \frac{\boldsymbol{j}_k}{\rho_k}\right) = \left(\frac{x_k}{R_u T}\right)(\nabla\mu_k + z_k F\boldsymbol{\Phi}) \tag{12}$$

where the chemical potential of species k is given by

$$\mu_k = \mu_k^0 + R_u T \ \ln\alpha_k \tag{13}$$

In Eq. (13), μ_k^0 is the standard-state chemical potential, and α_k is the activity of species k. The current density is calculated by summing the fluxes of all charge species:

$$\boldsymbol{i} = \sum_{k=1}^{N} \frac{z_k F \boldsymbol{j}_k}{M_k} \tag{14}$$

The electrolyte solution in AFCs consists of charge species (e.g., K^+, OH^-) and solvent (H_2O). Following Newman [7], the mass flux of species k is calculated by

$$\boldsymbol{j}_k = \left(\frac{t_k \rho Y_k \boldsymbol{i}}{z_k C_k F}\right) - \rho D_m \nabla Y_k + \rho Y_k \boldsymbol{v} \tag{15}$$

where t_k is the transference number

$$t_k = \frac{z_k^2 u_k C_k}{\sum_{j=1}^{N} z_j^2 u_j C_j} \tag{16}$$

The current density is calculated by

$$i = -\kappa\nabla\Phi - \sum_{k=1}^{N} z_k F D_k \nabla C_k \tag{17}$$

where κ is the KOH solution electrical conductivity

$$\kappa = \sum_{k=1}^{N} z_k^2 F^2 u_k C_k \tag{18}$$

and D_m is the KOH diffusion coefficient

$$D_m = \left(\frac{2D_+ D_-}{D_+ + D_-}\right) \tag{19}$$

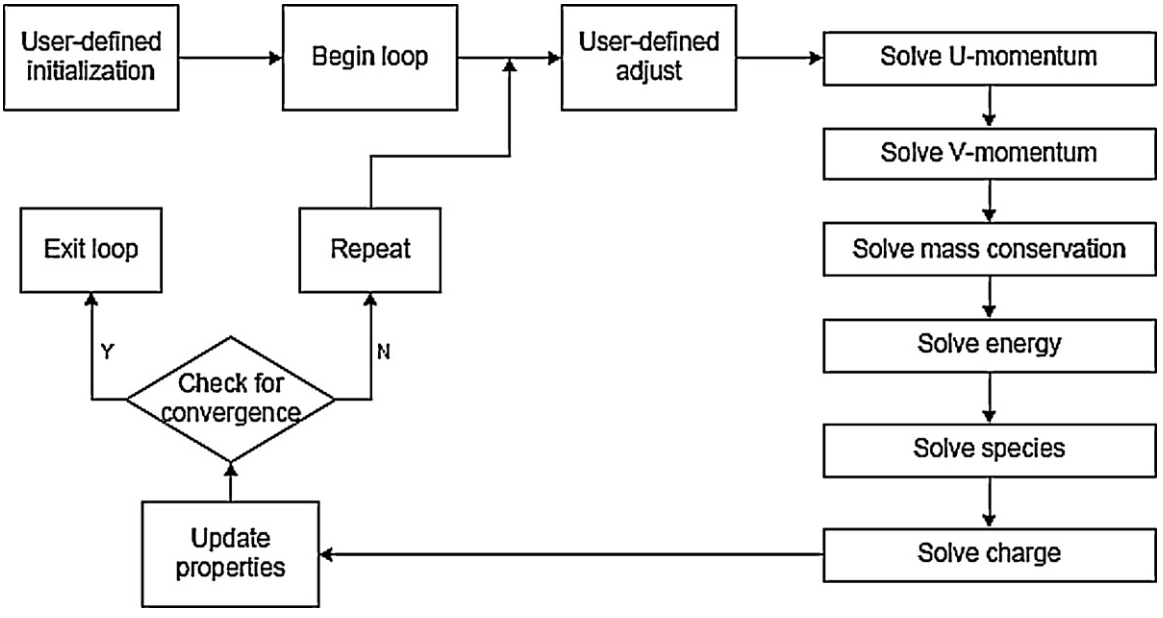

Fig. 2. Flowchart of CFD calculation.

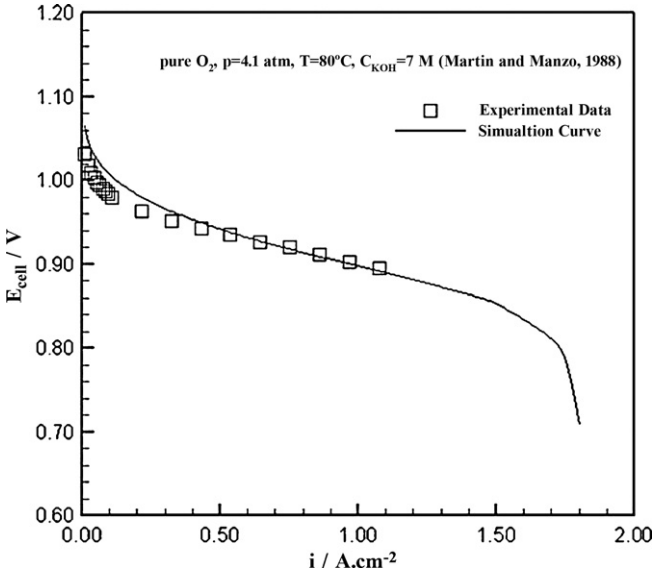

Fig. 3. Comparison of CFD calculation with experimental data [24].

where subscripts '+' and '−' denote the positive and negative ions, respectively.

For ideal solution, the Nernst–Einstein equation is used to calculate the mass diffusivity of species k

$$D_k = u_k R_u T \tag{20}$$

where

$$u_k = \frac{t_k \kappa_e}{z_k^2 \nu_k F^2 C_e}$$

2.4. Non-ideal solution

For non-ideal solution, the mass flux of species k is calculated by

$$\boldsymbol{j}_k = \frac{t_k \rho Y_k \boldsymbol{i}}{z_k C_k F} - \rho D_m \nabla Y_k + \rho Y_k \boldsymbol{v} \tag{21}$$

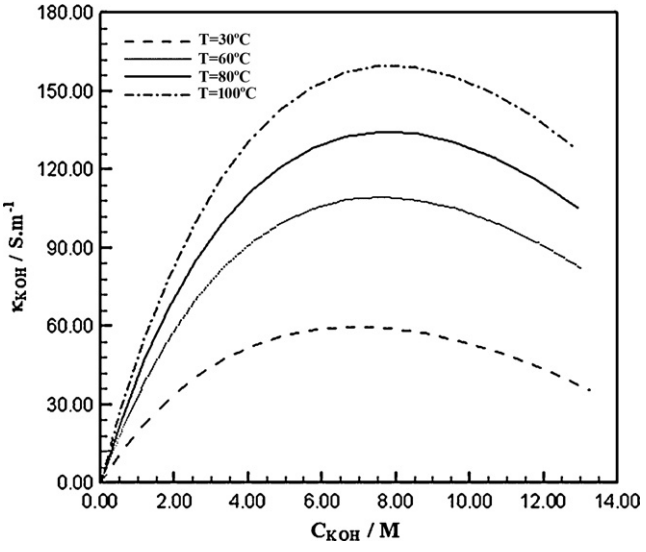

Fig. 4. KOH electrical conductivity as a function of KOH molarity; T = 20, 60, 80, 100 °C.

Table 4
Limiting ionic equivalent conductance [16].

Temperature (°C)	K^+ ($cm^2\ \Omega^{-1}\ mol^{-1}$)	OH^- ($cm^2\ \Omega^{-1}\ mol^{-1}$)
25	73.5	198.3
45	103.4	
55	119.2	
75	152.9	
100	195	450
125	240	

where

$$D_m = \left(\frac{DC_T M_0}{\rho}\right)\left(1 + \frac{d \ln \gamma_{\pm,C}}{d \ln C_e}\right) \tag{22}$$

$$D = \frac{D_{0+} D_{0-}(z_+ - z_-)}{z_+ D_{0+} - z_- D_{0-}} \tag{23}$$

$$C_T = C_+ + C_- \tag{24}$$

$$t_+ = \frac{\rho_0 t_+^0 + \rho_-}{\rho} \tag{25}$$

In Eqs. (22)–(25), D_{0+} and D_{0-} are the binary diffusion coefficient, C_e is the KOH concentration, C_T is the total molar concentration, $\gamma_{\pm,C}$ is the mean molar activity coefficient, and t_+^0 is the transference number. The dependency of transference number on electrolyte concentration is calculated by

$$\frac{t_i}{t_i^0} = \frac{\lambda_i^0}{\lambda_+^0 + \lambda_-^0} \tag{26}$$

where λ_i^0 is the limiting ionic equivalent conductance of ion i. The values of λ_i^0 at several selected temperatures are given in Table 4 [16]. The current density is calculated from

$$\boldsymbol{i} = -\kappa \nabla \Phi - \kappa^D \nabla \quad \ln C_e \tag{27}$$

where κ^D is the diffusion conductivity:

$$\kappa^D = \left(\frac{2R_u T \kappa}{F}\right)\left(1 - t_-^0 + \frac{C_e}{2C_0}\right)\left(1 + \frac{d \ln \gamma_{\pm,C}}{d \ln C_e}\right) \tag{28}$$

The non-ideal solution effects are calculated from the non-unity activity coefficients that appear in the species diffusion coefficients (Eq. (22)) and diffusion conductivity (Eq. (28)).

The primary and secondary (shunt) currents are calculated by the charge conservation equation. The source term in the charge equation is used to calculate the charge transfer between the solid and liquid phase. The Butler–Volmer equation is used to calculate the H_2 oxidation reaction (HOR) and O_2 reduction reaction (ORR) rates. An infinitely large electrical conductivity is assumed for the solid phase. Namely, the electrode is assumed to have an equipotential surface. Conversely, $\Phi_s = 0$ and $\Phi_s = E_{cell}$ are set for the anode and cathode, respectively.

A direct two-electron transfer reaction is assumed for HOR and a four-electron transfer reaction for ORR, e.g., Eqs. (1) and (2), respectively. The exchange current density is assumed to be 5.0×10^{-4} A cm^{-2} for HOR [17], and 5.0×10^{-8} A cm^{-2} for ORR [18]. The specific catalyst–electrolyte interface area, α_l, is estimated following Jo and Yi [13]. The specific gas–electrolyte interface area, α_g, and the thickness of the electrolyte film, δ_l, are specified using the reported values 10^5 m^{-1} and 10^{-1} μm, respectively [19,20]. The thickness of the GDL characteristic length, δ_g, is set to 10 μm [21]. The entropy changes of HOR and ORR are taken from [22]. The electrochemical parameters used in the calculation of the baseline condition are summarized in Table 5. The geometric parameters, along with the boundary conditions, are given in Table 6. Thermodynamic properties used in the calculation are listed in Table 7.

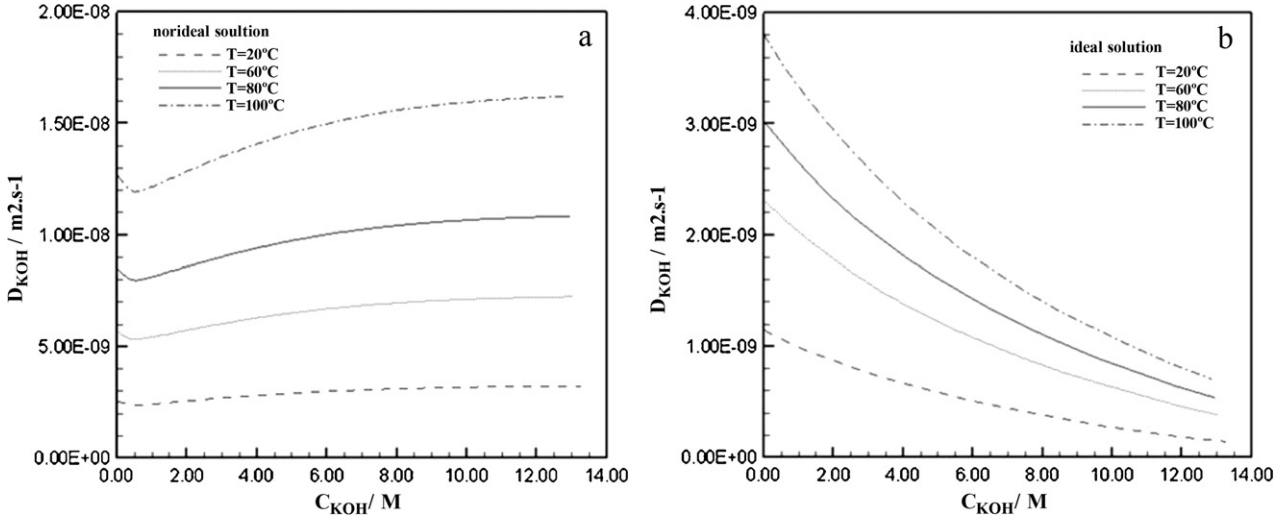

Fig. 5. KOH diffusion coefficient as a function of KOH molarity; T = 20, 60, 80, 100 °C; (a) non-ideal solution formulation, and (b) ideal solution formulation.

3. Solution method

3.1. Computational domain

The computational domain is divided into seven regions (domains) as illustrated in Fig. 1. Domains 1, 2, and 3 are the anode gas channel, gas diffusion layer (GDL), and catalyst layer, respectively. Domain 4 is the separator. Domains 5, 6, and 7 are the cathode catalyst layer, GDL, and gas channel, respectively. H_2 is transported from Domain 1 to Domain 2 by convection and diffusion, and dissolves in KOH solution. The dissolved H_2 reacts with hydroxide ions (OH^-) and forms H_2O at the anode catalyst layer (Domain 3). Electrons are released. The electrochemical reaction at the cathode catalyst layer (Domain 5) involves returned electrons from external circuit, dissolved O_2, and H_2O. O_2 is transported from Domain 7 to Domain 6, and dissolves in KOH solution. The OH^- ions are produced in Domain 5, carried away by diffusion, convection and migration actions, and consumed in Domain 3. The electrolyte flows through the separator (Domain 4); it also takes away the reaction heat and H_2O produced in Domain 3. Two extended channels (region: DEFG and OPQN) at separator inlet (edge: DG) and exit (edge: QN) are implemented to capture the external electrolyte flow.

3.2. CFD

FLUENT© was used to solve the coupled governing equations. The flow chart of the calculation procedure is illustrated in Fig. 2. The user defined functions (UDFs) were written to calculate the physical properties and the source terms for solving the governing equations, as well as to satisfy the prescribed boundary conditions. The graphical user interface (GUI) was used to input the UDFs to corresponding governing equations and the user defined scalar (UDS) was introduced to solve the charge equation. Two convergence criteria were enforced to ensure that (a) the local cell voltage is the same everywhere along the separator, and (b) the total current den-

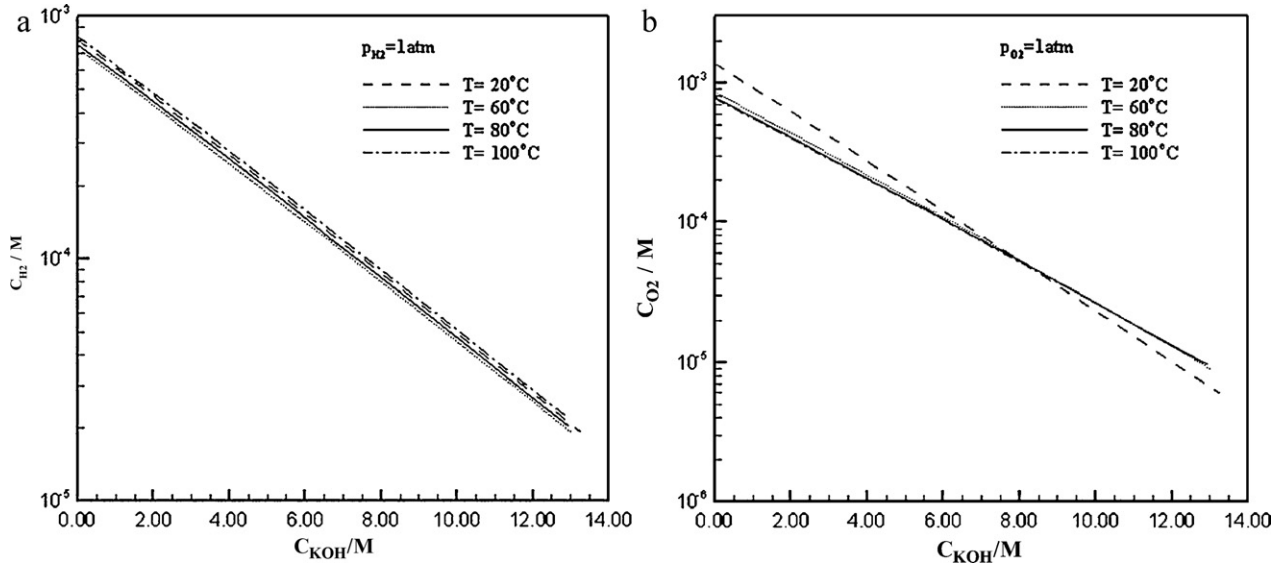

Fig. 6. Reactant solubility in KOH solution as a function of KOH molarity, T = 20, 60, 80, 100 °C, p = 1 atm; (a) H_2 and (b) O_2.

Table 5
Baseline conditions: electrochemical kinetic parameters for the anode and cathode.

Anode		Cathode	
Parameter	Value (unit)	Parameter	Value (unit)
n_a	2	n_c	4
s_{H_2}	1	s_{O_2}	−1
s_{OH^-}	2	s_{OH^-}	4
s_{H_2O}	−2	s_{H_2O}	−2
q_{H_2}	1	q_{O_2}	1
q_{OH^-}	2	q_{OH^-}	4
q_{H_2O}	2	q_{H_2O}	2
v_{K^+}	1	v_{K^+}	1
v_{OH^-}	1	v_{OH^-}	1
z_{K^+}	1	z_{K^+}	1
z_{OH^-}	−1	z_{OH^-}	−1
$\alpha_a^a n_a$	1.5	$\alpha_a^c n_c$	2.5
$\alpha_c^a n_a$	0.5	$\alpha_c^c n_c$	1.5
i_0^a	5.0×10^{-4} (A cm^{-2})[a]	i_0^c	5.0×10^{-8} (A cm^{-2})[b]
a_l^a	1.0×10^7 (m^{-1})[c]	a_l^c	1.0×10^7 (m^{-1})[c]
a_g^a	6.0×10^5 (m^{-1})[d]	a_g^c	6.0×105 (m^{-1})[d]
δ_l^a	1.0×10^{-7} (m)[e]	δ_l^c	1.0×10^{-7} (m)[e]
δ_g^a	1.0×10^{-5} (m)[f]	δ_g^c	1.0×10^{-5} (m)[f]
$C_{H_2}^r$	6.0913×10^{-7} (mol cm^{-3})	$C_{O_2}^r$	3.4905×10^{-7} (mol cm^{-3})
ΔS_a	161.2 (J mol^{-1} K^{-1})[g]	ΔS_c	-648.0 (J mol^{-1} K^{-1})[g]

[a] Tilak et al. [17].
[b] Kinoshita [18].
[c] Jo and Yi [13].
[d] Kenjo [19].
[e] Li et al. [20].
[f] Nam and Kaviany [21].
[g] Lampinen and Fomino [22].

Table 6
Baseline conditions: AFC structural parameters (*L*: thickness; *H*: height) and boundary condition.

Parameter	Value (unit)	Parameter	Value (unit)
$L_{separator}$	300 (μm)	$\varepsilon_{separator}$	1.0
L_{GDL}^a	250 (μm)	ε_{GDL}^a	0.7
L_{GDL}^c	250 (μm)	ε_{GDL}^c	0.7
L_{cat}^a	25 (μm)	ε_{cat}^a	0.7
L_{cat}^c	25 (μm)	ε_{cat}^c	0.7
$L_{channel}^a$	1 (mm)	τ_{GDL}^a	1.2
$L_{channel}^c$	1 (mm)	τ_{GDL}^c	1.2
$H_{separator}$	50 (mm)	τ_{cat}^a	1.2
$H_{separator}^{extended}$	50 (mm)	τ_{cat}^c	1.2

Inlet condition: C_e = 7 M, T = 80 °C, p = 4.1 atm; v^a, v^c, v^e = 0.2, 0.1, 0.01 m s^{-1}, RH = 0%.
Wall: adiabatic and impermeable, $\partial\phi/\partial n = 0$, ($\phi = T, Y_i, \Phi$).
Electrolyte inlet and exit: $\partial\Phi/\partial n = 0$.

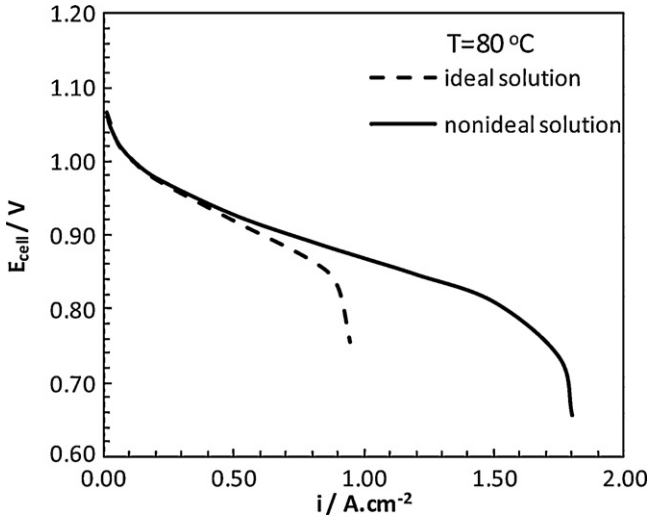

Fig. 7. Comparison of non-ideal solution versus ideal solution results: polarization curve, isothermal boundary condition.

sity equals that calculated by the specified, averaged cell current density.

4. Results and discussion

4.1. Validation

The CFD results of baseline condition (i.e., parameters specified in Tables 5 and 6) were validated by experimental data reported in [24]. The catalysts used in [24] were PtPd (loading at 10 mg cm^{-2}) and AuPt (loading at 20 mg cm^{-2}) for anode and cathode, respectively. The computation was performed to represent the operating condition: pure O_2 and pure H_2, 80 °C and 4.1 atm, and KOH concentration of 7 M. Excellent agreement (discrepancy less than 5%) was seen for current density greater than 0.30 A cm^{-2}, and good agreement (discrepancy less than 10%) for current density below 0.30 A cm^{-2}. The comparison is shown in Fig. 3. It should be noted that estimates were made on the parameters that were not available in the literature. These parameters are the effective liquid–solid surface area, the effective liquid–gas surface area, and the liquid diffusion film thickness. The calculation also showed that the cathode overpotential was the predominant loss mechanism that accounted for about 70% of the potential losses [27].

4.2. Property effects

The effects of thermodynamic and transport properties on AFC operation were examined. The electrolyte conductivity directly impacts the IR losses. The reactant dissolving rates can set the limiting current density condition. The KOH conductivity varies with temperature and molarity, e.g., see Fig. 4. At 80 °C, the conductivity peaks at around 7 M, which is the molarity condition chosen for AFC when operated at 80 °C [24]. Deviation from this molarity, for example, due to the presence of concentration gradient, will increase the IR losses and decrease the cell voltage.

The reactant (i.e., H_2 or O_2) dissolving rates are functions of reactant solubility, diffusion coefficients, specific gas–liquid interfacial

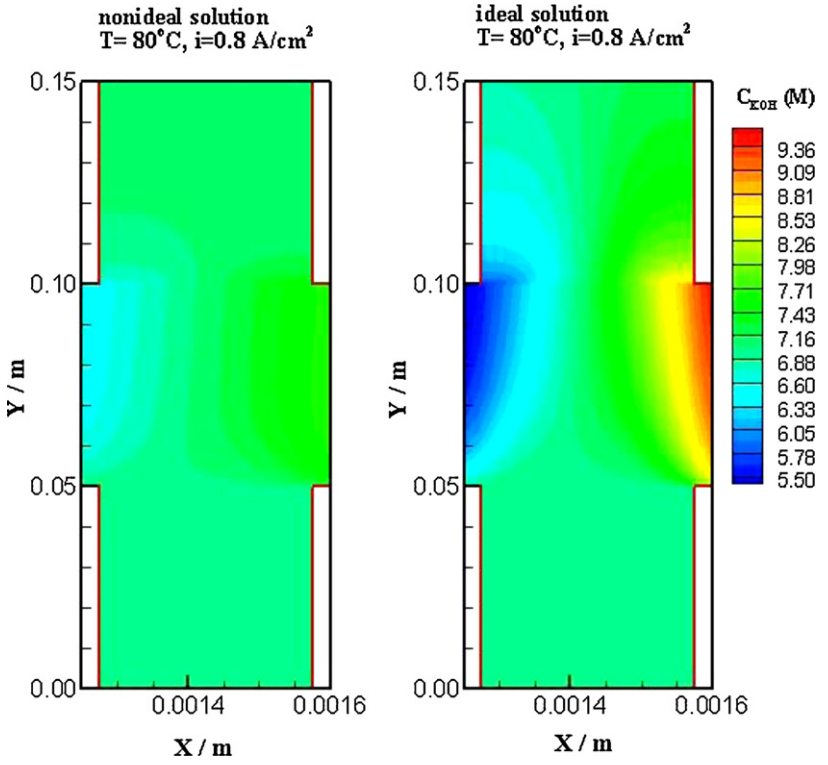

Fig. 8. Comparison of non-ideal solution versus ideal solution results: isopleths of KOH concentration in separator and extended channel; $i = 0.8\ \mathrm{A\,cm^{-2}}$; anode and cathode located at $x = 0$ and 0.0016 m.

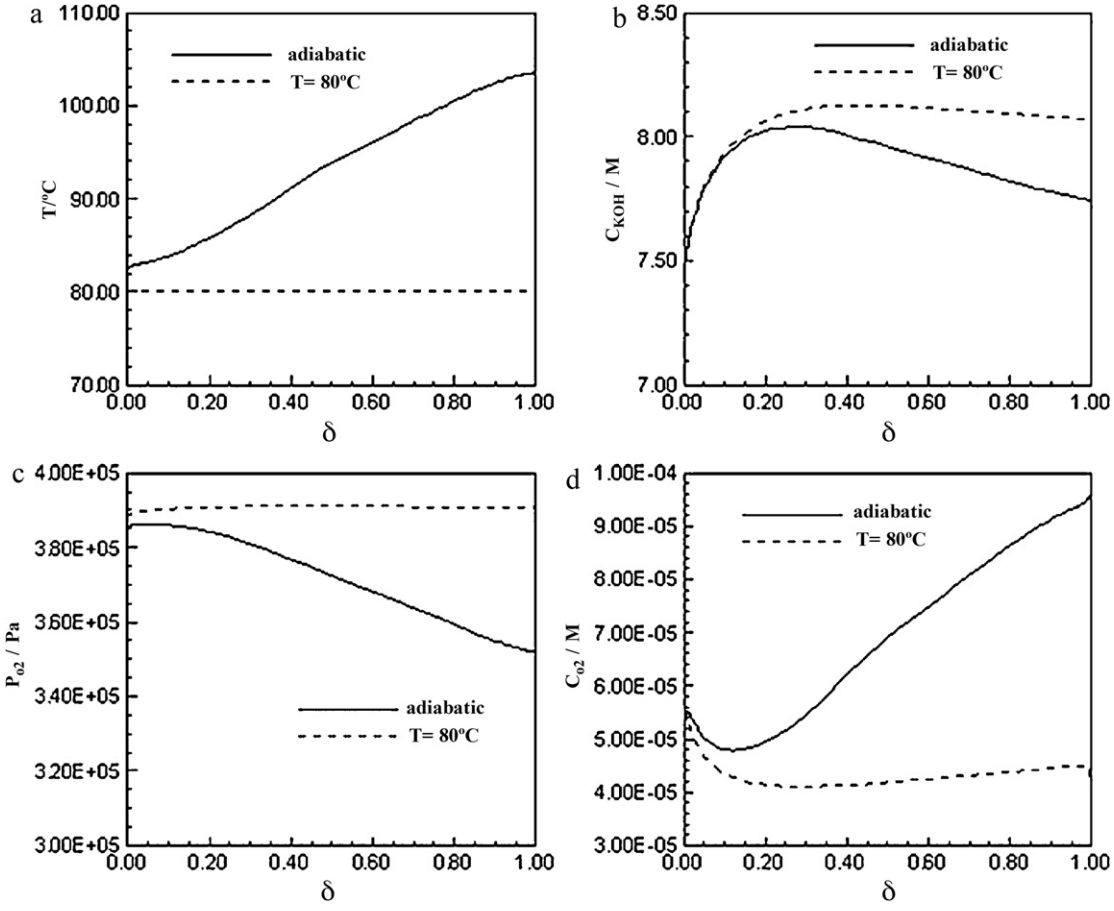

Fig. 9. Streamwise profiles at cathode–electrolyte interface of non-ideal solution formulation, $i = 1.5\ \mathrm{A\,cm^{-2}}$; δ is the dimensionless distance, inlet at $\delta = 0$ and exit at $d = 1$ and exit; (a) temperature, (b) KOH molarity, (c) oxygen partial pressure, and (d) dissolved oxygen molarity.

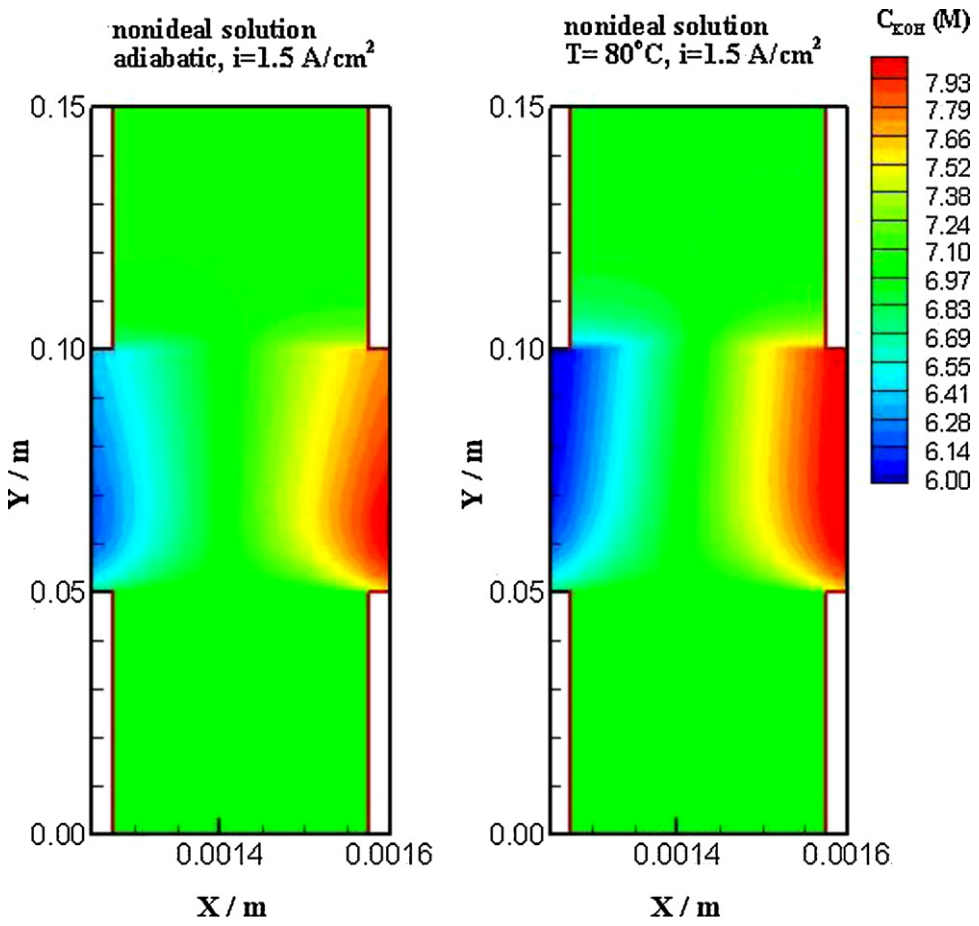

Fig. 10. Effects of adiabatic versus isothermal boundary condition on calculated isopleths of KOH concentration in separator and extended channel; $i = 1.5\ A\,cm^{-2}$, non-ideal solution formulation; anode and cathode located at $x = 0$ and 0.0016 m.

areas, and liquid film thickness. At constant temperature, the KOH diffusion coefficient reaches its minimum over the concentration range 0–1 M, e.g., see Fig. 5(a). The diffusion coefficient increases with increasing temperature and concentration. It increases by a factor of 6 when the temperature is increased from 20 to 100 °C, but the increase is less than 20% when the concentration is increased from 0 to 12 M. Also plotted in Fig. 5 is the calculated species diffusion coefficient when the ideal solution assumption is invoked, i.e., Fig. 5(b) for temperatures set to 20, 60, 80, or 100 °C. The comparison shows that when the ideal solution assumption is invoked it under-estimates the KOH diffusion coefficient and predicts an opposite trend with increasing KOH concentration when compared to the non-ideal solution results.

Solubility of H_2 and O_2 in KOH solution is of the same order of magnitude as shown in Fig. 6(a) and (b), respectively. Solubility decreases by about 2 orders of magnitude with increasing molarity over the range 0–12 M, but the change is much less with increasing temperature over the range 20–100 °C. In AFC, KOH is produced at cathode and consumed at anode, resulting in higher concentrations at cathode and lower at anode. Reaction therefore favors H_2 dissolution into KOH solution, and retards O_2 dissolution.

The presence of KOH concentration gradient across the electrolyte increases the IR losses when the concentration deviates from the design point of 7 M. To reduce the concentration gradient, one can increase the rate of KOH transport from cathode to anode, or increase the KOH flow rate. For a fixed fuel cell configuration, the former can be achieved by operating the fuel cell at higher temperatures to increase the diffusion coefficient (e.g., see Fig. 5(a)). However, increasing the temperature will also increase the H_2O evaporation rate, which in term will increase the KOH concentration and reduce O_2 solubility at cathode. The latter can be achieved at the expense of parasitic losses associated with the increase of the pumping power to re-circulate the electrolyte.

4.3. Ideal solution assumption

Isothermal boundary condition was chosen to examine the effects of ideal solution assumption on the calculation of polarization curves. Fig. 7 shows that when the ideal solution assumption is relaxed the calculated limiting current density is extended from 1.0 to $1.8\ A\,cm^{-2}$, which is a result of the increased diffusive transport of KOH in the electrolyte. As shown by the isopleths illustrated in Fig. 8, the ideal solution assumption results in concentrated KOH at cathode (in the range of 5.3–9.5 M for calculation with i set to $0.8\ A\,cm^{-2}$) and reduced KOH concentration at anode (in the range of 5.5–7.0 M). The non-ideal solution calculation, however, yields a more uniform KOH concentration (in the range of 6.4–7.7 M). These results can be explained by comparing the calculated diffusion coefficients given in Fig. 5(a) and (b). The value of diffusion coefficients calculated based on the ideal solution formulation, Fig. 5(b), was lower than that based on the non-deal solution formulation, Fig. 5(a). The diffusive transport of KOH from cathode to anode was lower with the ideal solution formulation. Consequently, higher KOH concentrations were predicted at cathode, which in term reduced the O_2 dissolving rate and lowered the limiting current density. As noted earlier, the maximum electrical conductivity occurs at KOH concentration around 7 M. A uniform KOH concentration around 7 M is expected to result in higher cell

Table 7
Thermodynamic properties.

Electrical conductivity (T in K; range: up to 9 M and above 0 °C) [16]:

κ_e (S cm^{-1}) = $0.0262W + 6.7\times10^{-4}W(T-273.15) - 4.8\times10^{-4}W^2 - 8.8\times10^{-6}W^2(T-273.15)$

Diffusion coefficient (C_e in mol cm^{-3}, T in K; range: up to 14 M and 90 °C) [28]:

D_m (cm^2 s^{-1}) = $\exp(-16.489 + 0.02015T - 8.1607C_e^{0.5} + 286.2C_e - 2539.8C_e^{1.5} + 7207.5C_e^2)$

Density (ρ in kg m^{-3}, m in mol kg^{-1} and T in K; range: up to 14 M and 100 °C) [29,30]:

$\rho = (2.11942\times10^3 + 1.03561\times10^2\ m - 3.67252\ m^2 + 9.30540\times10^{-2}\ m^3 - 1.11476\times10^{-3}\ m^4)\times T^{-0.13255}$

Activity coefficient (T in K range: m from 2 to 18 mol kg^{-1} and T from 0 to 200 °C) [31]:

$\gamma_{\pm,C} = \gamma_{\pm,m}(\rho_{H_2O}/(\rho_e - M_eC_e))$; $\log\gamma_{\pm,m} = 473.520 - 76.168/T - 8.1727T + 0.05818T^2 - 2.1864\times10^{-4}T^3 + 4.5717\times10^{-7}T^4 - 5.0464\times10^{-10}T^5 + 2.2960\times10^{13}T^6 - (0.079599 - 51.367/T)\ m + (0.44109 - 88.190/T)\ \log m$

Specific heat (T in K; range: 25–150 °C) [32]:

C_p (J kg^{-1} K^{-1}) = $2358.948 + 2.0934T$

Thermal conductivity (C_e in mol L^{-1}; $a_1 = -7.19\times10^{-4}$, $a_2 = -1.0\times10^{-4}$; range: 1–16 M) [33]:

$\lambda_{38\,^\circ C}$ (kcal m^{-1} h^{-1} k^{-1}) = $0.538 + a_1C_e + a_2C_e^2$; $(\lambda_T/\lambda_{38\,^\circ C})_{soln} = (\lambda_T/\lambda_{38\,^\circ C})_{H_2O}$

λ_{H_2O} (W m^{-1} K^{-1}) = $1.487188\times10^{-8}T^3 - 1.143515\times10^{-5}T^2 + 2.193975\times10^{-3}T + 0.559401$; T in °C

Dynamic viscosity (T in °C; range: 3–11 M and 10–60 °C) [34]:

μ (kg m^{-1} s^{-1}) = $(1.71468\times10^{-2} - 1.02529\times10^{-1}W + 2.72493\times10^{-1}W^2)T^{-0.5414}$

Gas solubility in electrolytes (k_{scx} in m^3 kmol^{-1}; range: 25–100 °C) [12,13,35]:

$\log(x_i^0/x_i) = k_{scx}C_e$; $k_{scx,H_2} = 0.129$; $k_{scx,O_2} = -4.1315\times10^{-8}T^3 + 1.4405\times10^{-5}T^2 - 1.5914\times10^{-3}T + 2.1139\times10^{-1}$

$C_k = He_kp_k$; $He_k = (C_0 + 2C_e)(x_k/(1-x_k))$; C_0 : *solvent*, C_e : *salt*

Gas solubility in pure H_2O (H in kmol m^{-3} atm^{-1}; Henry's law) [36]:

$\log H^* = -(1.142 - 2.846(1/T)^* + 2.486(1/T)^{*2} - 0.9761(1/T)^{*3} + 0.2001(1/T)^{*4})$

$H^* = H/H_{max}$; $(1/T)^* = (1/T - 1/T_r)/(1/T_{max} - 1/T_r)$; $T_r = 647$ K (critical temperature of water)

$H_{max}\times10^{-4} = 7.08\ (O_2),\ 7.54\ (H_2),\ 12.39\ (N_2)$; $(1/T_{max})\times10^3 = 2.73(O_2),\ 3.09(H_2),\ 2.80(N_2)$

Diffusion coefficient of dissolved gases (D in cm^2 s^{-1}; range: KOH up to 15 M, 25–100 °C) [37]:

$D^l_{H_2} = (1.3004\times10^{-6} - 8.4347\times10^{-6}Y^{0.5} + 2.7822\times10^{-5}Y - 4.1593\times10^{-5}Y^{1.5} + 2.2415\times10^{-5}Y^2)T^{1.28968}$

$D^l_{O_2} = (5.5421\times10^{-7} - 2.3393\times10^{-6}Y^{0.5} + 6.3923\times10^{-6}Y - 9.6313\times10^{-6}Y^{1.5} + 5.4576\times10^{-6}Y^2)T^{1.20838}$

Vapor pressure (p in bar, T in K; range: 0–300 °C KOH up to 25 mol kg^{-1}) [38,39]:

$\log p_w = a + b\log p_w^0$; $a = (-1.508m - 1.6788m^2 + 2.25887\times10^{-3}m^3)\times10^{-2}$, $b = 1 - (1.2062m + .56024m^2 - 7.8228\times10^{-3}m^3)\times10^{-3}$

$\log p_w^0 = 35.4462 - 3343.93/T - 10.91\ \log T + .0041645T$

Electrode thermal conductivity [25,26]:

$\lambda_a = \lambda_c = 1.5$ W m^{-1} K^{-1}

voltages when operated in the IR dominated regime, e.g., see Fig. 8 for the results of current density in the range 0.4–0.8 A cm^{-2}. The property considerations suggest that maintaining a uniform KOH concentration in the electrolyte, for example at 7 M, be a design strategy to extend the limiting current density condition, and to reduce the IR losses in AFC.

4.4. Thermal boundary conditions

To examine the effects of thermal conditions on the calculation of polarization curves, the baseline condition of isothermal boundary condition (at 80 °C) was changed to one subject to adiabatic boundary condition. One major effect of the adiabatic boundary condition was that it increased the cathode temperature along the streamwise direction from 82 °C at inlet ($\delta = 0$) to just above 100 °C at exit ($\delta = 1$), see Fig. 9(a). As discussed earlier, O_2 solubility is relatively insensitive to temperature change over the range studied, cf., Fig. 6(b); however, the dissolved O_2 level was orders of magnitude higher at the exit, Fig. 9(d). The oxygen partial pressure was about two orders of magnitude lower at the exit, e.g., see Fig. 9(c). The higher dissolved O_2 level was due to the higher KOH diffusion coefficient calculated by the adiabatic boundary condition. The diffusion coefficient increased by an order of magnitude when the temperature was increased from 80 to 100 °C, cf. Fig. 5(a). The KOH transport rate from cathode to anode was increased accordingly, and it resulted in lower KOH concentrations at the cathode, Fig. 9(b). The isopleths of the results subject to adiabatic and isothermal boundary conditions are illustrated in Fig. 10. For isothermal condition, the KOH concentration remained high along the cathode (i.e., along the y-direction at $x = 0.0016$ m) and low along the anode (i.e., along the y-direction at $x = 0.00$ m). The growth of the concentration layer was reminiscent to that of the boundary-layer flow. However, this was not the case for the adiabatic boundary condition. The increase of diffusion coefficient along the cathode helped to transport away KOH to anode. The thickness of the concentration boundary decreased, the KOH concentration decreased, and dissolved O_2 level increased. The net effects are that the adiabatic boundary condition extended the limiting current density from 1.8 to 2.3 A cm^{-2} (cf., Fig. 11). It is also noted that both thermal

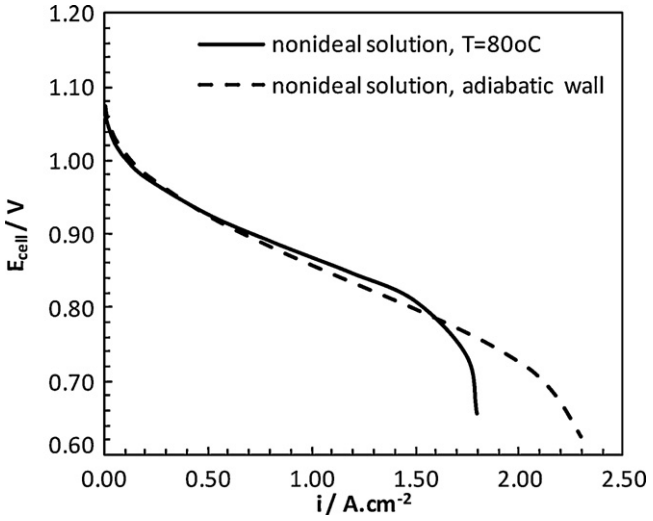

Fig. 11. Effects of adiabatic versus isothermal boundary condition on calculated polarization curve; non-ideal solution formulation.

conditions yielded similar cell voltages for $i < 1.6\,A\,cm^{-2}$, although the adiabatic boundary condition predicted a significantly higher limiting current density.

5. Summary and conclusion

A computational investigation was conducted that relaxed the ideal solution assumption, and accounted for thermodynamic solubility of the reactants and property variations due to the temperature effects. For the condition studied, at which the cathode overpotential accounts for about 70% of the cell potential losses, the following conclusions can be drawn:

1. The ideal solution formulation underestimates the limiting current by about 50%. This level of discrepancy suggests that the ideal solution assumption should not be applied in the modeling and simulation of AFC for conditions similar to that considered in this study.
2. The thermal condition can significantly change the results of the calculation. The adiabatic boundary condition can increase the limiting current by 30%. Conversely, thermal management can significantly extend the limiting current condition, thus increase the power density of the fuel cell.
3. The computational results showed that a nearly uniform distribution of KOH in the electrolyte was responsible for the higher limiting current density condition calculated in the study. Conversely, a design strategy to yield a uniform KOH concentration in the electrolyte (e.g., at the design point of 7 M) will be an effective measure to increase the limiting current density condition.

Acknowledgment

This research was supported, in part, by ConocoPhillips.

References

[1] K. Kordesch, K. Tomantschger, F. Mcclusky, J. Power Sources 18 (1986) 317–335.
[2] K. Kordesch, V. Hacker, J. Gsellmann, J. Power Sources 86 (2000) 162–165.
[3] K. Strasser, J. Power Sources 29 (1990) 149–166.
[4] E.D. Geeter, M. Mangan, S. Spaepen, J. Power Sources 80 (1999) 207–212.
[5] T. Burchardt, P. Gouerec, E.S. Cortezon, Fuel 81 (2002) 2151–2155.
[6] G.F. McLean, T. Niet, S. Prince-Richard, N. Djilali, Int. J. Hydrogen Energy 27 (2002) 507–526.
[7] J.S. Newman, Electrochemical Systems, Englewood Cliffs, New Jersey, 1973.
[8] R.F. Probstein, Physicochemical Hydrodynamics: An Introduction, Butterworths, Boston, 1989.
[9] M.A. Al-Saleh, S. Gultekin, S. Rahman, A. Al-Zakri, J. Power Sources 55 (1995) 33–39.
[10] S.C. Yang, P. Bjornbom, Electrochim. Acta 37 (1992) 1831–1843.
[11] S. Rowshanzamir, M. Kazemeini, M.K. Isfahani, Int. J. Hydrogen Energy 23 (1998) 499–506.
[12] M.C. Kimble, R.E. White, J. Electrochem. Soc. 138 (1991) 3370–3382.
[13] J.H. Jo, S.C. Yi, J. Power Sources 84 (1999) 87–106.
[14] S.G. Bratsch, J. Phys. Chem. Ref. Data 18 (1989) 1–22.
[15] R.B. Bird, W.E. Stewart, E.N. Lightfoot, Transport Phenomena, second ed., John Wiley & Sons, New York, 2002.
[16] A.L. Horvath, Handbook of Aqueous Electrolyte Solutions: Physical Properties, Estimation and Correlation Methods, Ellis Horwood, England, 1985.
[17] B.V. Tilak, P.W.T. Lu, J.E. Colman, S. Srinivasan, J.O'M. Bockris, in: B.E. Conway, E. Yeager, R.E. White (Eds.), Comprehensive Treatise of Electrochemistry, vol. 2, Plenum Press, New York, 1984, pp. 18–24.
[18] K. Kinoshita, Electrochemical Oxygen Technology, Wiley, New York, 1992.
[19] T. Kenjo, J. Electrochem. Soc. 133 (1986) 2051–2058.
[20] Q.F. Li, G. Xiao, H.A. Hjuler, R.W. Berg, N.J. Bjerrum, J. Electrochem. Soc. 141 (1994) 3114–3119.
[21] J.H. Nam, M. Kaviany, Int. J. Heat Mass Transfer 46 (2003) 4595–4611.
[22] M.J. Lampinen, M. Fomino, Chem. Technol. Metall. Ser. 213 (1993) 1–45.
[23] L.M. Litz, K.V. Kordesch, in: G.J. Young, H.R. Linden (Eds.), Fuel Cell Systems, American Chemical Society, Washington, 1965, pp. 167–187.
[24] R.E. Martin, M.A. Manzo, Energy Convers. Eng. Conf. (1988) 301–304.
[25] A. Rowe, X.G. Li, J. Power Sources 102 (2001) 82–96.
[26] J. Ramousse, J. Deseure, O. Lottin, S. Didierjean, D. Maillet, J. Power Sources 145 (2005) 416–427.
[27] G. Zhou, Modeling and simulation of electrolyte transport in alkaline fuel cells, Ph.D thesis, University of Iowa, Iowa City, 2007.
[28] P. DeVidts, J. Delgado, B. Wu, D. See, K. Kosanovich, R.E. White, J. Electrochem. Soc. 145 (1998) 3874–3883.
[29] G. Akerlof, P. Bender, J. Am. Chem. Soc. 63 (1941) 1085–1088.
[30] O. Sohnel, P. Novotny, Densities of Aqueous Solutions of Inorganic Substances, Elsevier, New York, 1985.
[31] J. Balej, Collect. Czech. Chem. Commun. 61 (1996) 1549–1562.
[32] D.M. Ginzburg, V.E. Kochkalda, N.I. Guba, Russ. J. Phys. Chem. 47 (1973) 1214–1215.
[33] Z. Losenicky, J. Phys. Chem. 73 (1969) 451–452.
[34] I.N. Maksimova, S.V. Sergeev, J. Appl. Chem. USSR 47 (1974) 1712–1714.
[35] S.K. Shoor, R.D. Walker, K.E. Gubbins, J. Phys. Chem. 73 (1969) 312–317.
[36] D.M. Himmelblau, J. Chem. Eng. Data 5 (1960) 10–15.
[37] M.K. Tham, R.D. Walker, K.E. Gubbins, J. Phys. Chem. 74 (1970) 1747–1751.
[38] J. Balej, Int. J. Hydrogen Energy 10 (1985) 233–243.
[39] E. Schmidt, U. Grigull, Properties of Water and Steam in SI-Units, second ed., Springer, Berlin, 1982.